JOM, Vol. 72, No. 3, 2020
https://doi.org/10.1007/s11837-020-04014-w

THE 2ND ASIA-PACIFIC INTERNATIONAL CONFERENCE ON ADDITIVE MANUFACTURING (APICAM 2019)

PolyJet 3D Printing of Composite Materials: Experimental and Modelling Approach

YUN LU TEE,[1] CHENXI PENG,[1] PHILIP PILLE,[2] MARTIN LEARY,[3] and PHUONG TRAN [1,4]

1.—School of Civil and Infrastructure Engineering, RMIT University, Melbourne, VIC 3000, Australia. 2.—Advanced Manufacturing Precinct, RMIT University, Melbourne, VIC 3000, Australia. 3.—School of Mechanical and Automotive Engineering, RMIT University, Melbourne, VIC 3000, Australia. 4.—e-mail: jonathan.tran@rmit.edu.au

Multi-material 3D printing has created a wide range of applications because of its high-resolution and multi-functional capabilities. It is important to understand the interaction of the materials both macroscopically and microscopically. This article investigates the mechanical responses of rigid-rubbery polymeric material fabricated using the PolyJet technique as an individual constituent and as an integrated composite unit cell. A series of experiments were conducted to obtain the mechanical responses for individual VeroMagentaV (rigid) and Agilus30 (flexible) polymers with different shore-hardness levels. Tensile results show that the interface of the dual material is strong enough to withstand the stretching during the tensile experiment. The interfacial hardness and local elastic modulus in dual-material parts investigated using nano-indentation and visual inspections showed distinct transition properties. The introduction of different types of rigid reinforcement particles of the 3D-printed composite has been demonstrated and quantified. A numerical model is developed, and the results show good agreement with the compression experiments.

INTRODUCTION

Additive manufacturing (AM), from the early stage of single material rapid prototyping, is currently going through a huge transition, transforming into multi-material printing with unprecedented design opportunities.[1,2] Coupled with different printing technologies, the fabrication of digital computer-aided designs (CAD) for physical 3D objects is achievable within a short duration. Multi-material AM has created a new possibility, which enables one-step production of 3D-printed composite materials. Different from traditional manufacturing processes, which could only produce a simple geometry, 3D printing has greatly extended its capability in design complexity. Multi-material AM includes multiple metals, ceramics and polymers. It also involves cross materials such as metal and ceramics.[3] Nevertheless, multi-material printing is still in its infancy compared with the single material printing technology.

Among the various 3D printing technologies from fused deposition modelling (FDM), stereolithography (SLA) and selective laser sintering (SLS), PolyJet by Stratasys stands out from the others. This is due to the uniqueness of this technology, which allows the user to have a high-resolution part made with a wide selection of material properties.[3] Moreover, this printer can be installed in ordinary room conditions and does not require a specialised laboratory environment (although ventilation/air scrubbing is recommended).[4] PolyJet printing utilises inkjet technology with accuracy up to 14 μm vertical resolution of layer thickness deposited from a 1200 DPI nozzle. The high accuracy is achieved by multiple nozzles spraying tiny droplets onto the build area, which are then instantaneously exposed to UV light for each layer. The complex geometry may be supported by a thin raft and encasing of the part in support material, which can be easily removed upon completion. Supporting material can be removed by manual peeling, WaterJet or

(Published online January 27, 2020)

soaking in sodium hydroxide (NaOH) solution (although NaOH has been shown to damage the gloss finish of parts).[5]

Some parameters affect the mechanical responses of 3D-printed structures, such as the composition, printing directions/orientation, surface finishing, ageing and lighting condition.[3,6–10] Cazon et al.[8] found that the orientations and surface roughness of the prints have a significant influence on the mechanical properties. Bass et al.[11] found that specimens aligned parallel to the printing direction are stronger than those in the transverse direction. While most of the literature presented the mechanical responses of 3D-printed materials, having an understanding from the microstructural point of view is of equal importance. Dealing with 3D-printed parts that involve more than one material, the interface is one of the major aspects to be considered. Traditional composite materials exhibit two distinct boundaries that induce the composite to fail at the interface layer because of delamination. At present, several technologies have been reported having the capability to produce a functionally graded material (FGM) composite, including FDM, SLS and PolyJet.[12,13] The material distribution at the interface is not widely explored. Mueller et al.[6] found that multi-material prints fail at both the interface and within the material. Moore et al.[14] revealed that there were many voids in the rubber-like material TangoBlack, between 25 and 30 μm in size. Voids in the material act as a stress concentration and lead to material failure. Lumpe et al.[15] found that the strength of the interface is affected by the printing parameters and material combination. In their work, a combination of VeroWhite, a rigid material, and TangoBlackPlus, a rubbery material, resulted in both interface and material failure. No significant failure trend was concluded.

Significant effort is given in AM aiming to produce parts with outstanding mechanical properties.[16] Composite materials are favourable because of their combination of mechanical properties; however, they are relatively new to AM.[17] Dimas et al. reported that the fracture behaviour of 3D-printed composites has significant toughening and stable crack propagation.[18] Dalaq et al. showed that different types of triply periodic minimal surfaces (TPMS) as a reinforcement resulted in different mechanical behaviours.[19] While the effect of PolyJet's processing parameters has been explored, the study of composite material by this technology is limited.[20]

Several studies have been conducted on Vero and TangoBlack.[7,11,15,21–27] However, Stratasys recently introduced a rubber-like photopolymer, Agilus30, which has superior tear resistance and tensile strength compared with TangoBlack.[28] This motivated the study of the mechanical interactions between Vero and Agilus30. As the material is relatively new to the market, Agilus30 has not been extensively studied.

Different shore hardness material phases could be designed and combined simultaneously to achieve the desired composite properties. The use of particles or short fibres as reinforcements with different shapes, sizes and volume fractions in polymer matrix composites is a common approach in various industrial and consumer applications (e.g., automotive, electronics, biomedical). From the properties of single materials characterised from experiments, accurate predictions of the deformation and failure behaviour of the corresponding composite are important for a reliable product design. Finite element analysis (FEA) methodology is the most commonly used tool to validate and predict behaviours of composite materials. Its accuracy depends on the development of adequate material models characterised by reliable input material parameters. In PolyJet applications, due to the large-scale deformation behaviour of the elastomers (Agilus30), the hyperelastic material model[29,30] is often utilised. There is still very limited research linking PolyJet individual materials and its composite structures, especially when considering the influences of the constituent volume fraction, distributions and number of material phases.

This article aims to investigate the interactions of 3D-printed bi-material from two perspectives: the macro- and micro-scale levels. From the macro-scale, tensile and compression tests are conducted; from the micro-scale, a nanoindentation test is performed. The fracture surface is visually inspected using an optical microscope as an initial approach to fractography study. The article is arranged as follows: Methods section depicts the fabrication of the test samples and the methodology involved. The findings obtained are presented in the Results and Discussion section. Numerical simulations are presented in the Numerical Validation section as validation of the experimental work. The article ends with the summarised outcomes of this work.

METHODS

Material Design and Fabrication

Stratasys J750 (Stratasys Ltd.) was used in the fabrication of all samples. This printer consists of four inkjet heads depositing from eight reservoirs, which are linked to material print cartridges; two UV light sources cure the photosensitive resin as one roller runs over the samples layer by layer.[31,32] The printer is operated with GrabCAD Print software to load the stereolithography (STL) files and to assign printing material to each sample. Upon completing each printing batch, the jetting nozzles are cleaned with isopropyl alcohol to prevent material build-up.

Two types of materials, VeroMagentaV (RGD852) and Agilus30(FLX935), were chosen to fabricate all the testing samples. VeroMagentaV is a rigid material containing low-viscosity acrylic oligomer, 4-(1-

oxo-propenyl)-morpholine, exo-1,7,7-trimethylbicyclo [2,2,1] hept-2-yl acrylate and (octahydro-4,7-methano-1H-indenediyl) bis(methylene) diacrylate. VeroMagentaV from the VeroVivid™ family was chosen as a visibly distinct colour from Agilus30, which was preferable for the interface study described later in this research. Agilus30 is a rubbery material made from acrylic monomer, exo-1,7,7-trimethylbicyclo [2.2.1] hept-2-yl acrylate and Genorad 20. Support material is automatically generated when assigning materials to the samples. The rafts are made from support material (SUP706B) containing acrylic acid, 2-hydroxyethyl ester and n-hydroxyethlacrylamide. Samples were printed with a gloss top surface finish, with the base having a matte finish because of the support material raft required to adhere the part to the build platform.

Tensile specimens were designed according to the ASTM D638 standard[33] with slight variation in line with the dimensions presented by Lumpe et al.[15] as shown in Fig. 1a and b. For a homogeneous sample, the overall length, LO, is 63.5 mm, and the overall width, WO, is 11.0 mm. The gauge length, G, is 18 mm, and the radius at the boundary, R, is 12.7 mm. The width, W, is 6.0 mm. All the measurements are the same for heterogeneous samples, with an exception at the gauge section, L, of 10 mm to assign a different material.

Three different categories were produced. First, homogeneous samples of VeroMagentaV (VMV) and Agilus30 (A30) were printed to understand the characteristics of the individual materials. This group of samples was printed in both parallel and transverse directions to the printhead as shown in Fig. 1d. Next, heterogeneous samples with VMV on both extended ends and Agilus-based materials at the gauge section were fabricated. Only parallel printing was considered for all heterogeneous cases. A variety of different shore hardness gradients (SH) was used in the gauge section of the tensile samples. The different shore hardness gradient gauges were assigned via the GrabCAD Print software. For example, on a VMV-A30 sample, the gauge section was assigned a single material, A30, having a shore hardness of 30. For VMV-A30_SH40, the gauge section was a mixture of a high-volume fraction of A30 and low volume fraction of VMV, having a shore hardness of 40. For VMV-A30_SH95, the gauge section was made up of a low volume fraction of A30 and high-volume fraction of VMV. Each set of the samples differed according to the shore hardness at the gauge section, ranging from 30, 40, 60, 70 to 95. Due to different volume fractions, samples with different shore hardnesses can be distinguished visually by the magenta intensity. Acronyms were assigned based on the materials on both extended ends of the sample, the gauge material and the shore hardness, namely VMV-A30, VMV-A30_SH40, VMV-A30_SH60, VMV-A30_SH70 and VMV-A30_SH95. In addition to shore hardness variation, a preliminary case study of hybrid tensile samples was also included (Fig. 1c). Having similar presentation as a VMV-A30 sample, the gauge

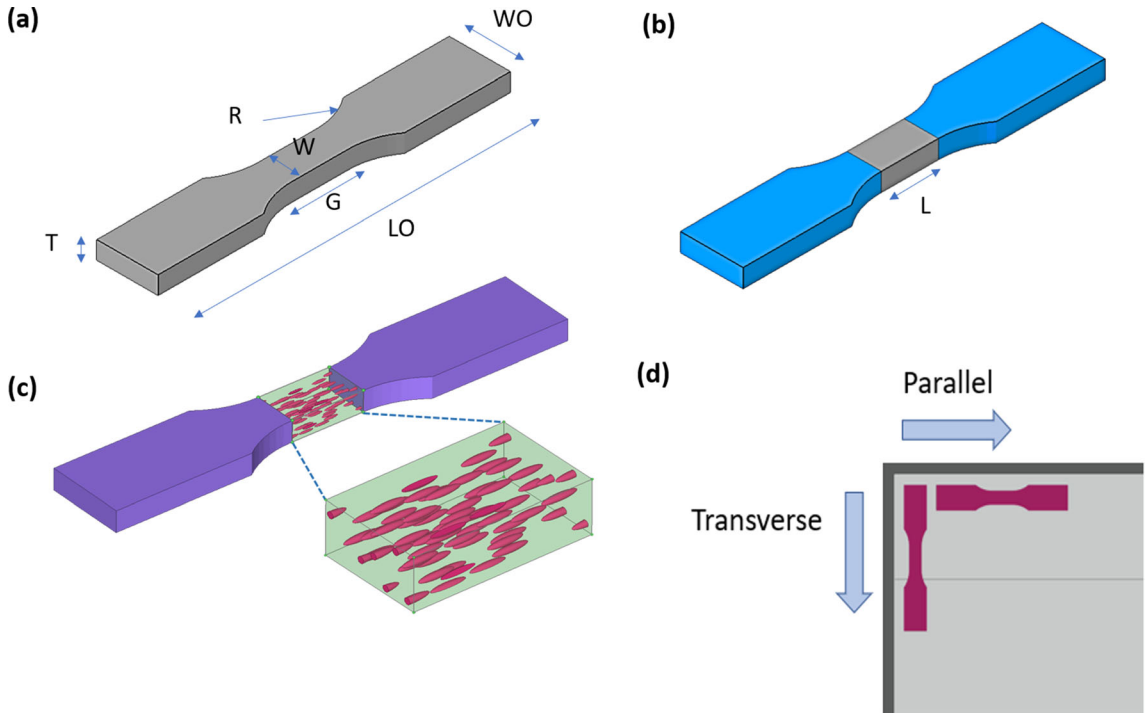

Fig. 1. Schematic diagram of (a) homogeneous sample and (b) heterogeneous sample and (c) hybrid samples. (d) Printing directions of the samples.

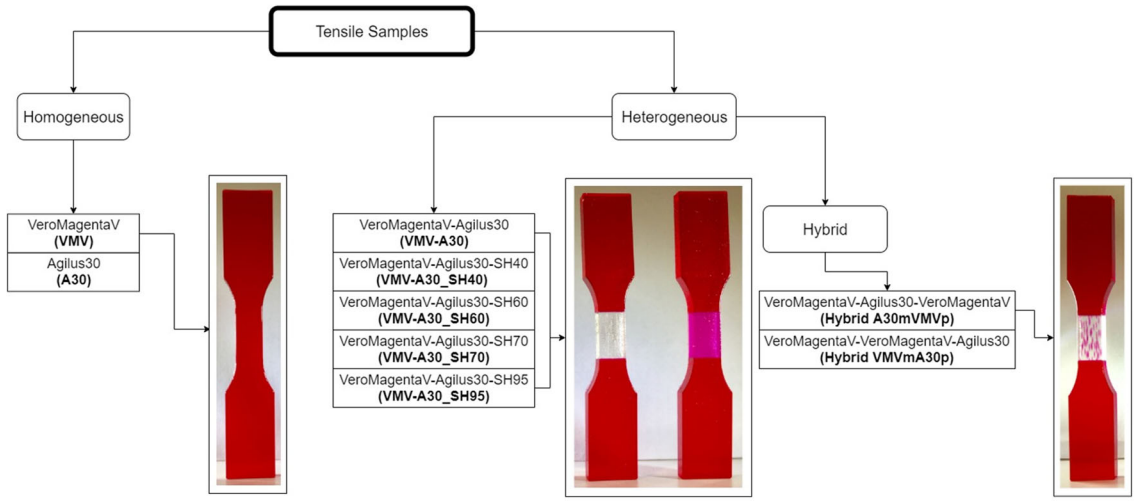

Fig. 2. List of tensile samples used in the experimental work and the corresponding 3D-printed ones. For the hybrid A30mVMVp sample, character "m" denotes matrix and character "p" denotes particles. Five per cent of VMV particles are randomly distributed in the hybrid A30mVMVp's gauge section, and 5% A30 particles are randomly distributed in the hybrid VMVmA30p's gauge part.

section has an additional inclusion of 5 vol.% of ellipsoidal particles aligned parallel to the printing direction. Two variations were produced: first, the gauge section with A30 as the matrix and VMV as the particles (hybrid A30mVMVp); second, the VMV as the matrix and A30 as the particles (hybrid VMVmA30p). Figure 2 shows the list of tensile samples and acronyms that will be used throughout this article.

Composite materials are used in various mechanical loading conditions. In addition to tensile characteristics of bi-material 3D printing, compression properties of 3D-printed parts were also investigated. Prior to the study of mechanical responses of composite compression samples, the compression behaviour of A30 was investigated. A diabolo-shaped compression sample was designed with a diameter of 13 mm at the centre and height of 35 mm as shown in Fig. 6d. This will be used as the reference material in Numerical Validation section. Next, cubical composite compression samples with 30 mm height, 30 mm length and 30 mm width were designed with Autodesk NetfabbBasic software with the introduction of 10% particles by volume. Three different types of particles were chosen as the infills, including spherocylindrical, spherical and ellipsoidal. The VMV particles were aligned randomly within the cubical A30 matrix. To avoid matte surfaces on the samples, the CAD models were designed such that an extra 0.5 mm of A30 is covered on the surface. To avoid significant warpage, a 30-mm square base with 2 mm height was added to the base. A schematic diagram of the composite compression samples and 3D-printed samples is shown in Fig. 3.

To better understand the local mechanical properties via nanoindentation testing, a rectangular interface sample was produced that was 2 mm thick, 15 mm wide and 20 mm long (10 mm VeroMagentaV and 10 mm Agilus30). All the above-mentioned samples were initially cleaned by manual peeling off the raft followed by a WaterJet to remove the residual supporting material attached to the samples. They were air-dried at room temperature.

Experimental Work

Chemical Composition Analysis

The Fourier transform infrared spectroscopy (FTIR) (Perkin Elmer Spectrum 100) technique was used to analyse the chemical composition of VeroMagentaV and Agilus30. All the spectra were measured at a spectral resolution of 4 cm^{-1}, with 32 scans taken per sample.

Differential scanning calorimetry (MDSC) 2920 from TA Instruments was used to investigate the glass transition temperature T_g of A30 and VMV. Modulus differential scanning calorimetry (MDSC) was used to investigate the thermal behaviour under low temperature (-60°C) to high temperature (400°C). The temperature was initially jumped to -60°C and increasing heat by 2°C per min.

Mechanical Analysis

The Instron 4465 machine with a 5-kN load cell was used to conduct tensile tests with a displacement control of 1 mm/min. Five samples were tested for each combination. Compression tests were conducted on the cubic composite samples with rate of 1.3 mm/min using Instron 5900R with a load cell of 30 kN. The compression test was conducted up to 30% and three samples were tested for each case.

The nanoindentation technique was used to measure the localised mechanical properties of materials, particularly the elastic modulus and

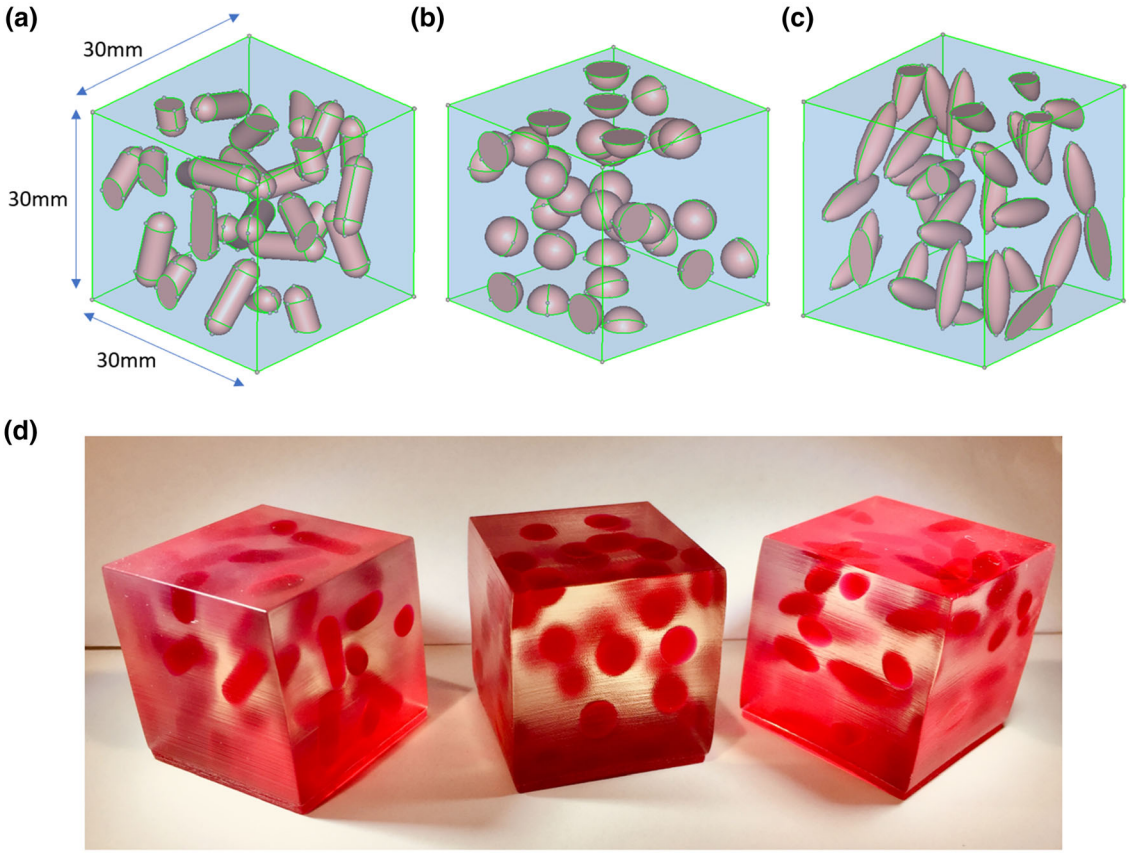

Fig. 3. Schematic diagram of composite compression samples with different type of reinforced particles: spherocylindrical (a), spherical (b) and ellipsoidal (c). Corresponding 3D-printed composite compression samples are presented in (d).

hardness.[34,35] A Hysitron TI 950 NanoIndenter machine was used to perform nanoindentation on the interface material. A hardness test was performed on the interface samples to provide a better understanding of the change in hardness levels across two different materials. A 5-μm Berkovich indenter tip was used throughout the hardness test, with 50-μN load. The hardness of the two materials, VeroMagentaV and Agilus30, was investigated, with special focus on the interface between the two distinct materials.

Visual Inspection

Visual inspection was performed using a Keyence VHX 5000 digital optical microscope, with a large depth of field used to inspect the fracture surface of tensile samples at 50× magnifications. In addition, a Leica DM2500M microscope was used to obtain a closer view at both glossy and matte surfaces of the tensile samples. Images were captured at 5×, 10× and 20× magnifications.

RESULTS AND DISCUSSION

Chemical Composition Analysis

Figure 4 shows the spectrum of VeroMagentaV and Agilus30. They show qualitatively similar chemical compositions despite their physical appearance at room temperature. The height difference between the two samples suggested that the materials are different quantitatively. The samples have a high fingerprint region from 600 cm^{-1} to 1500 cm^{-1}. The spectrum shows that both materials are acrylic based, (C=O) at 1721 cm^{-1}. Based on the

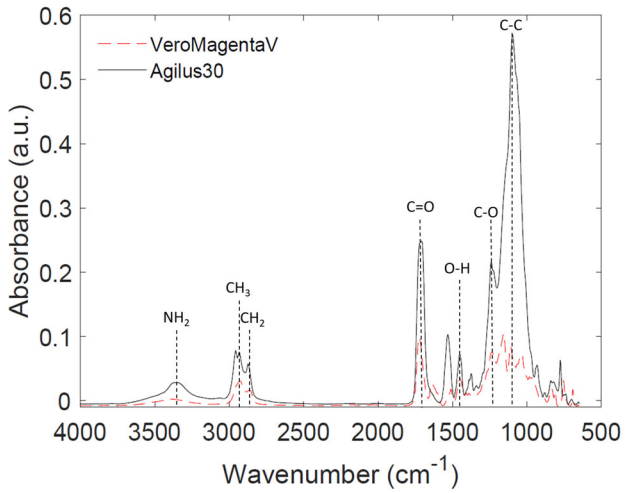

Fig. 4. FTIR analysis of VeroMangentaV and Agilus30.

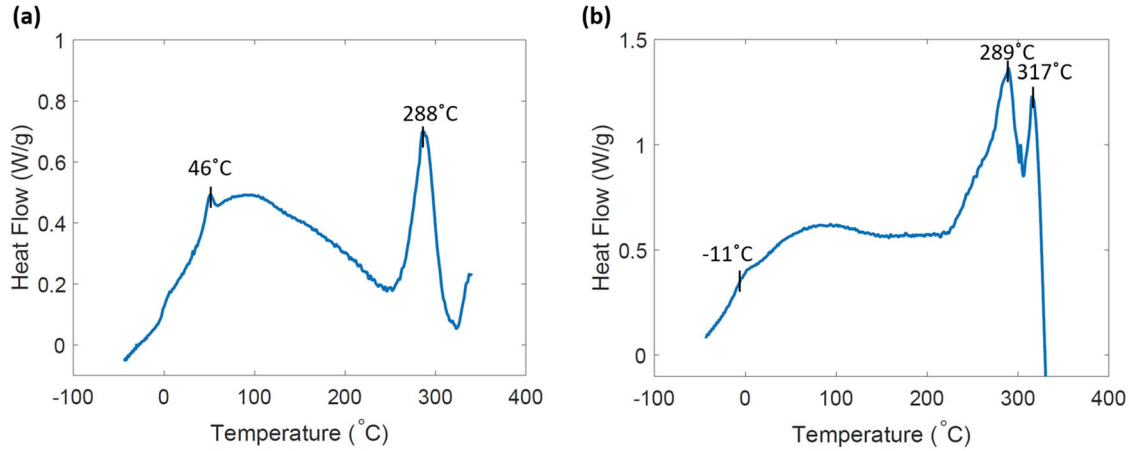

Fig. 5. DSC analysis of (a) VeroMagentaV and (b) Agilus30.

contents given by the manufacturer, the major difference is the existence of Genorad 20 in Agilus30, which is a polymerisation inhibitor.[36]

DSC analyses of VMV and A30 are shown in Fig. 5. The glass transition temperatures, T_g, obtained for VMV and A30 are 46°C and -11°C, respectively. Melting temperature for VMV is 288°C. There are two melting temperatures for A30, 289°C and 317°C, respectively. This could be two polymers with similar melting temperatures as the material is made of a mixture of different chemicals.

Mechanical Testing

To have a better understanding of the mechanical properties and nonlinear behaviours of PolyJet's materials, we conducted a series of standard tensile and compression experiments on single and bi-material printed parts. Stress–strain curves obtained from this section will be used as input for numerical validations.

Figure 6a shows the stress–strain response of hybrid A30mVMVp, homogeneously A30-printed in the parallel and transverse directions. Despite being printed in two different directions, there is no significant change in the tensile strength. Hybrid A30mVMVp, a sample consisting of VMV particles at the gauge section, exhibited a lower strain due to the shorter A30 region at the gauge section. Compared with VMV-A30 (the sample with no particles at the gauge section), the hybrid sample with an inclusion of 5% reinforcement resulted in higher stiffness. Conversely, the ultimate tensile stress is lower for the hybrid A30mVMVp. Figure 6b shows the stress–strain curves of the homogeneous VMV and hybrid VMVmA30p. Similar to the homogeneous A30 samples, different printing directions do not affect the tensile strength of the materials. It is worth noting that the curves show a stress delay region at the onset of the tensile test. This phenomenon only occurs on homogeneous VMV printed in both parallel and transverse directions. Hybrid VMVmA30p shows a slightly lower strength due to the weaker A30 inclusions within the gauge section. In the case of different shore hardnesses in the gauge section (Fig. 6c), it clearly shows that higher shore hardness resulted in higher ultimate tensile strength, where the effect is dominated by the higher content of VMV. VMV-A30_SH95 has a high composition of the rigid VMV to A30 ratio. The resulting stress–strain curve is dominated by the rigid VMV, experiencing high ultimate tensile strength. On the other hand, samples with lower shore hardness exhibited similar stress–strain curves like for homogeneous A30 samples. All tensile samples failed within the gauge section (details are shown in "Visual Observations" section). No delamination at the interface is observed. This shows that the samples have a strong interface between the two distinct materials. Tensile samples were printed with glossy finishing; however, the base, which was built using an automatically generated raft, left a matte surface. During tensile testing, cracks were initiated at the matte surface and led to final failure. (The glossy surface is achieved by continued exposure to the UV lamp; perhaps the matte base surface does not have much exposure.) This issue is unavoidable because of the laying-flat orientation of the samples during printing.

A cylindrical compression sample of A30 single material shows lower compression strength than reinforced composite compression samples (Fig. 6d). Higher compression strength is found on spherocylindrical followed by ellipsoidal and spherical reinforced particles. Spherocylindrical particles, in addition to their tubular shape, have a higher contact area in the A30 matrix. This resists the local movement of the matrix, resulting in higher strength. This phenomenon is similar for ellipsoidal particles, which have smaller contact areas than spherocylindrical particles. Cracks started to appear when the spherocylindrical composite sample was compressed up to 30%. Particles along the

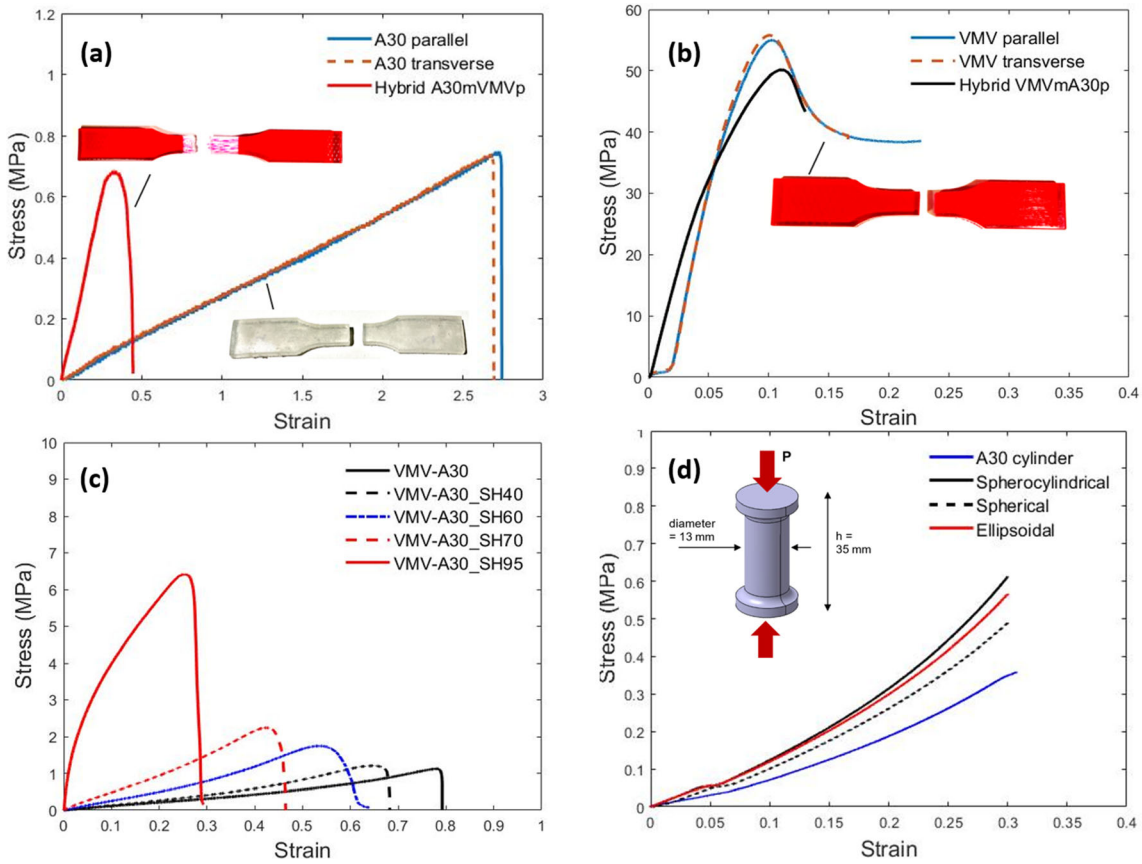

Fig. 6. (a) Stress–strain curves of A30 in two different directions (parallel, transverse) and hybrid sample (hybrid A30mVMVp). (b) Stress–strain curves of VMV in two different directions (parallel, transverse) and hybrid sample (hybrid VMVmA30p). (c) Stress–strain curves of samples with different gauge compositions (A30, A30_SH40, A30_SH60, A30_SH70 and A30_SH95). (d) Stress–strain curves of A30 cylinder and composite compression samples with different reinforcement particles (spherocylindrical, spherical and ellipsoidal).

surface started to delaminate. For ellipsoidal and spherical composite cubes, no delamination occurred. The shorter particles make a lower contribution to resisting deformation. Local buckling occurred at the edge of the samples for all three cases during the compression test, as shown in Fig. 12e, governed by the hyperelastic nonlinearity of the material. Nonlinearity was observed in the initial stage of the experimental stress–strain curves. This may be caused by the slightly uneven surface at the bottom of the sample due to the concave warpage of A30. A 2-mm VMV base was included to reduce the effect of warpage; however, the issue could not be solved completely because of the nature of this material.

Nanoindentation

Figure 7 shows the hardness and elastic modulus contour of the VMV and A30 interface. The blue regions indicate A30 and the green–red regions indicate VMV. The hardness value at the A30 region is found to be approximately 10 MPa. As the indenter moves towards the boundary, the hardness value increases to approximately 24 MPa. At the VMV region, the hardness generally falls in the range of 40-70 MPa, with some exceptions in several locations that reach up to 90 MPa. Referring to Fig. 7b, the elastic modulus contour gives a better illustration of the transition of the materials. Upon crossing A30, there is an intermediate phase between 2 and 3 GPa. This region clearly shows that the indenter has crossed the A30 region followed by a gradual increase in elastic modulus. As the indenter continues to move forward, the elastic modulus increases up to the maximum value, confirming that this is a VMV region. The localised modulus is found to be higher than the data obtained from the manufacturer. This finding is in agreement with the results reported by Muller et al.[7]

Visual Observations

Fractured surfaces of the tensile samples were observed under an optical microscope with 50× magnification, as shown in Fig. 8. All samples have one matte surface because of being attached to the build platform. Concave warpage from the direction of the base is observed across Agilus-based samples, whereas VMV samples have a flat base with sharp flat edges at the bottom. While conducting the tests, cracks appeared on the matte surface and propagated until final failure. Stretching of the rubber-

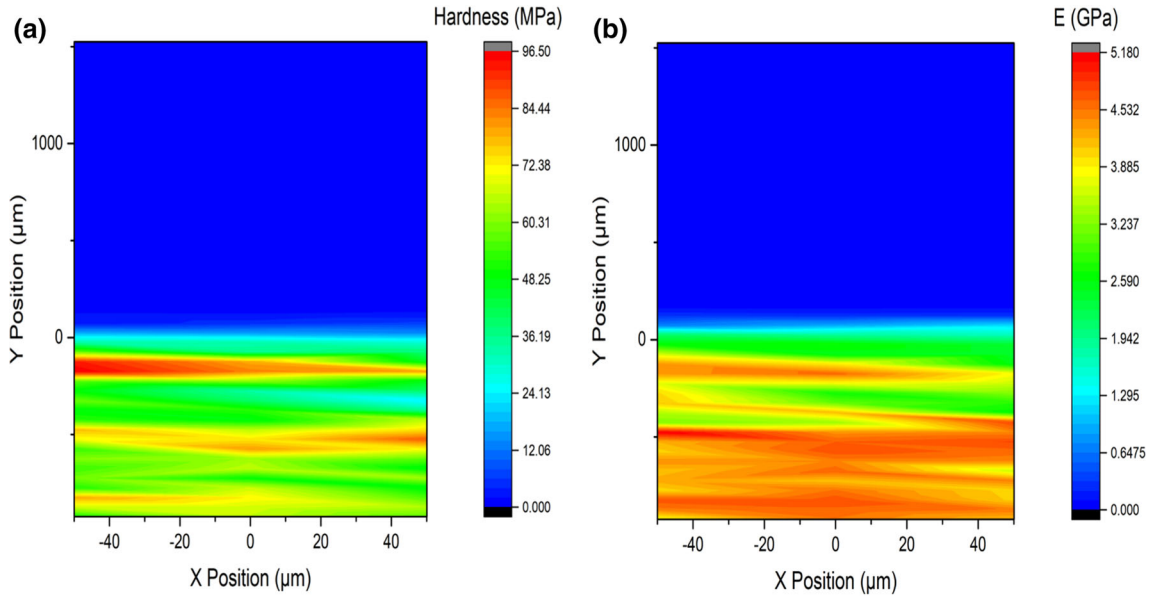

Fig. 7. (a) Hardness contour map and (b) Young's modulus contour map of the interface between Agilus30 and VeroMagentaV.

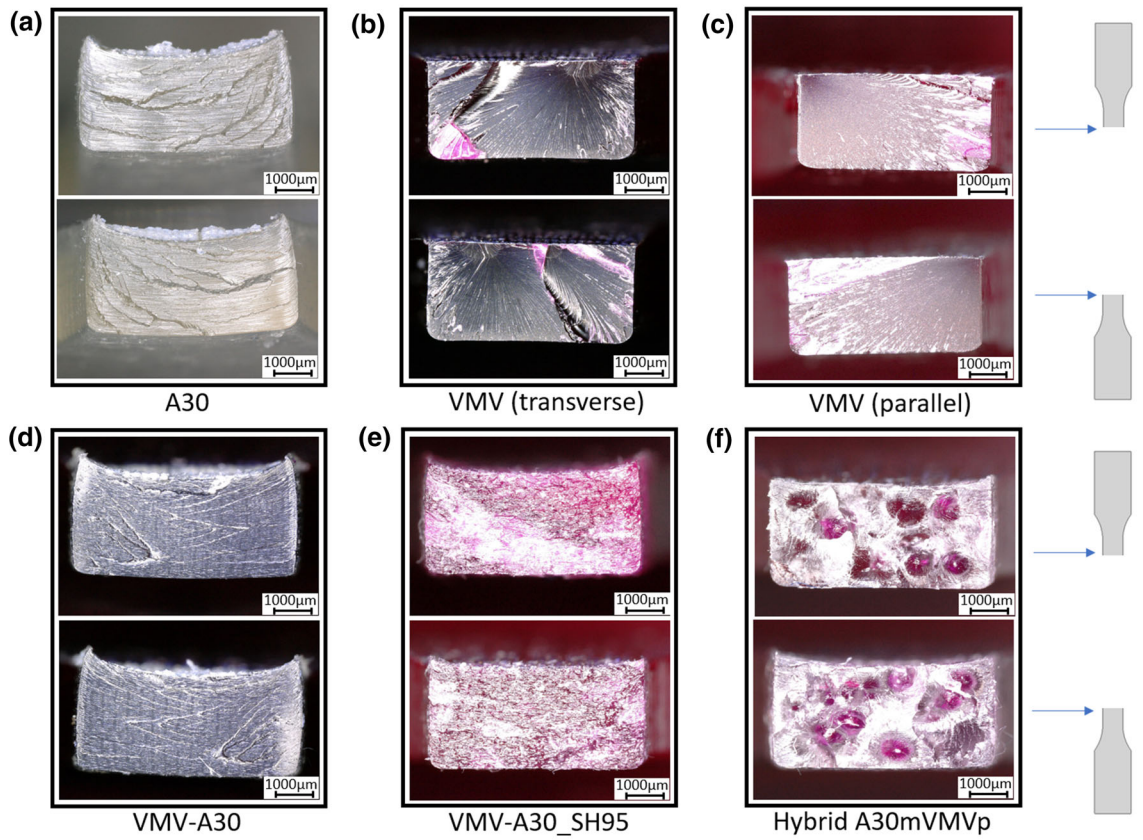

Fig. 8. Upper and lower fracture surfaces of various tensile samples. (a) A30; (b) VMV (transverse); (c) VMV (parallel); (d) VMV-A30; (e) VMV-A30_SH95; (f) hybrid A30mVMVp. All images were captured at 50× magnifications.

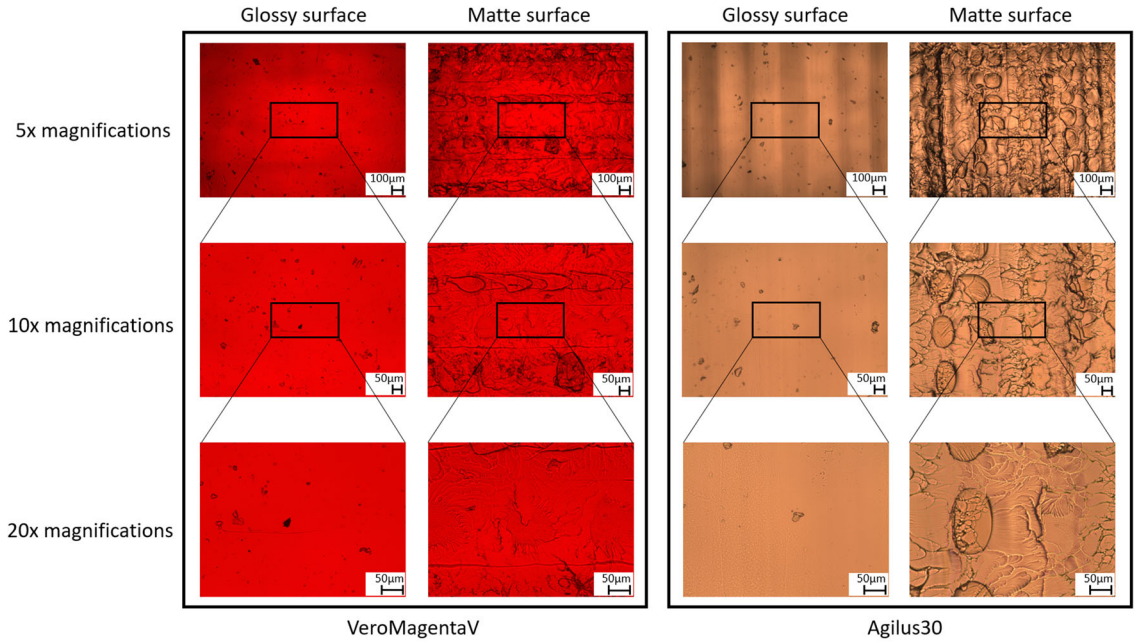

Fig. 9. Glossy (top) surface and matte (bottom) surfaces of VeroMagentaV and Agilus30 under optical microscope at 5×, 10× and 20× magnifications, respectively.

like homogeneous A30 (Fig. 8a) caused multiple cracks along the gauge section. The crack initiation and propagation processes are relatively long compared with VMV, which breaks instantaneously upon reaching maximum load. By observing the fracture surface of VMV printed in the parallel direction (Fig. 8b), the cracks were directed from a semi-circular notch initiated along the matte surface. Compared with the VMV in transverse direction (Fig. 8c), cracks initiated from the edge of the matte surface. Figure 8d has a similar fracture surface as the homogeneous A30 sample, having a wavy surface and multiple cracks. Figure 8e, which has a mixture of A30 and VMV contents, leaves a shiny fracture surface due to the higher content of rigid and vivid VMV. Figure 8f shows the surface of a failed hybrid A30mVMVp. Compared with other failures, the surface of a hybrid sample yields an uneven surface. With ellipsoidal particles aligning parallel along the sample, some of the VMV particles were broken while some only detached at the tip of the particles.

Raft is needed to fix the sample to the build platform, leaving the bottom of the sample a matte surface, while the top surfaces remain glossy. Cracks often initiated from the matte (bottom) surface instead of glossy (top) surface. Figure 9 shows the images of the VeroMagentaV and Agilus30 surfaces under optical microscope at 5×, 10× and 20× magnifications. Compared with glossy surfaces, matte surfaces show droplets created from the nozzles. Referring to images at 5× magnifications, droplet alignment is based on the printing orientations, where VMV is printed in parallel and A30 is printed in transverse direction. Boundaries of the droplets are observed on matte surfaces at 10× magnifications. Taking a closer view at 20× magnifications, fine lines are noticeable across the matte surfaces. In contrast, the glossy surface remained smooth, with only some voids. Due to the contrast between glossy and matte surfaces, we can deduce that cracks initiate from the uneven matte surface leading to final failure.

NUMERICAL VALIDATION

Numerical Model

The development of 3D-printed composite structures using the PolyJet technique presented in the previous section provides an opportunity to tailor the mechanical properties of composite materials by incorporating reinforced particles. In this study, the Agilus30 matrix (A30) is reinforced with different types of VeroMagentaV (VMV) particles of different shapes (spherocylindrical, spherical, ellipsoidal) at the volume fraction of 10%. The objective of this numerical section is to develop a numerical model for this composite structure to capture the large and nonlinear deformation that can then validate the experiments. Tensile and compressive experimental data for individual material, presented in previous sections, are utilised to calibrate the material model. In particular, the mechanical responses of 3D-printed reinforced composites under uniaxial compression are numerically investigated by finite element modelling implemented in ABAQUS/Standard 2018 (Simulia, Providence, RI). The cubic matrix is made of A30, while VMV-reinforced particles are distributed randomly inside the matrix at equivalent 10% volume fraction. Imperfections

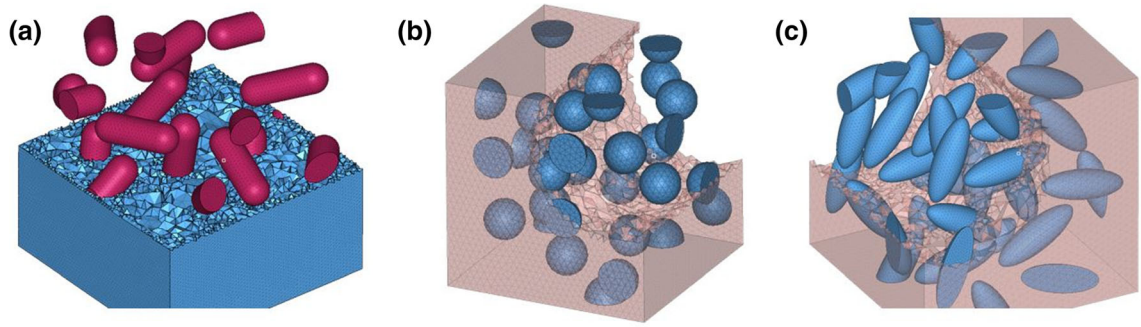

Fig. 10. Fine finite element mesh considered for numerical simulations of three cases: (a) spherocylindrical reinforcement; (b) spherical reinforcement; (c) ellipsoidal reinforcement. Snapshots of FE mesh and cross-section views to show the VMV particles embedded in the A30 matrix with node matching interface.

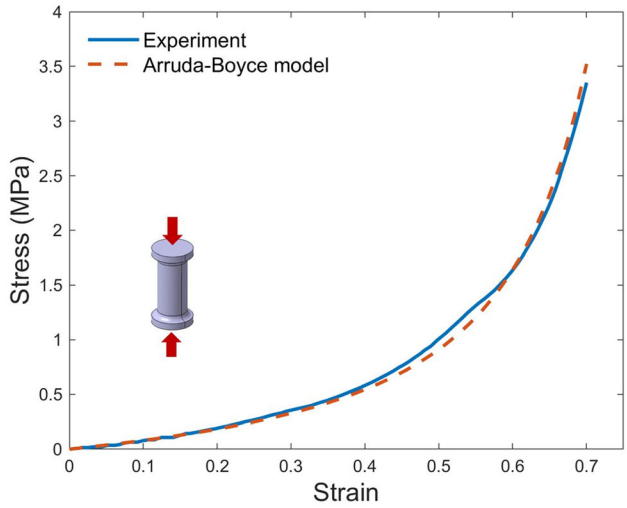

Fig. 11. Calibration of the Arruda-Boyce hyperelastic model by uniaxial compression.

caused by 3D printing are not considered in this study, and A30 and VMV are considered to bond perfectly at the interface. In this study, the A30 matrix is modelled by 574,502 four-node linear tetrahedron, hybrid, linear pressure C3D4H elements, while the VMV particles are discrete with 119,279 four-node linear tetrahedron C3D4 elements to ensure that the numerical results are independent of mesh density as shown in Fig. 10. For spherocylindrical and ellipsoidal reinforced particle cases, care must be taken with the mesh around the tips of particles, which have high curvature, to avoid the excessive element distortion during simulations. Particles are meshed with 0.2-1-mm elements depending on the curvature.

The engineering stress–strain data of A30 and VMV from the uniaxial compression and tension test are adopted to characterise the material model in the simulation. The mechanical property of VMV is simplified to be elastic-perfectly plastic with elastic modulus of 858 MPa and yield strength of 57.5 MPa obtained from experimental results. The constitutive model of A30 is described based on the Arruda-Boyce hyperelastic model,[37] given by,

$$U = \mu\left\{\frac{1}{2}(\bar{I}_1 - 3) + \frac{1}{20\lambda_m^2}(\bar{I}_1^2 - 9) + \frac{11}{1050\lambda_m^4}(\bar{I}_1^3 - 27) + \frac{19}{7000\lambda_m^6}(\bar{I}_1^4 - 81) + \frac{519}{673750\lambda_m^8}(\bar{I}_1^5 - 243)\right\} + \frac{1}{D}\left(\frac{J_{el}^2 - 1}{2} - \ln J_{el}\right), \quad (1)$$

where U is the strain energy density; μ, λ_m and D are the material parameters; $\bar{I}_1$ is the first deviatoric strain invariant; J_{el} is the elastic volume ratio. The stress–strain data from uniaxial compression are fitted by the Arruda-Boyce model, as shown in Fig. 11. The mechanical responses of A30 are approximated as a non-compressible hyperelastic material with an initial shear modulus, μ, of 0.238 MPa and locking stretch, λ_m, of 2.059. It is assumed that all the VMV particles are perfectly bonded with the A30 matrix. Thus, tie constraints are imposed to the interfaces between the matrix and particle parts. To simulate the uniaxial compression, two rigid plates are created. A normal contact behaviour is defined between the composite specimen and rigid plates by hard contact formulation, while penalty friction formulation with a friction coefficient of 0.3 is applied to describe the tangential behaviours. A uniaxial quasi-static displacement loading equivalent to engineering strain of 0.3 is applied on the top plate, while all the translations and rotations of the bottom plate are fixed.

Numerical Results

The numerical results are extracted and compared with experimental ones in Fig. 12a–d. Good agreements between numerical simulations and experiments are observed for all the cases, and more importantly localised buckling behaviours of

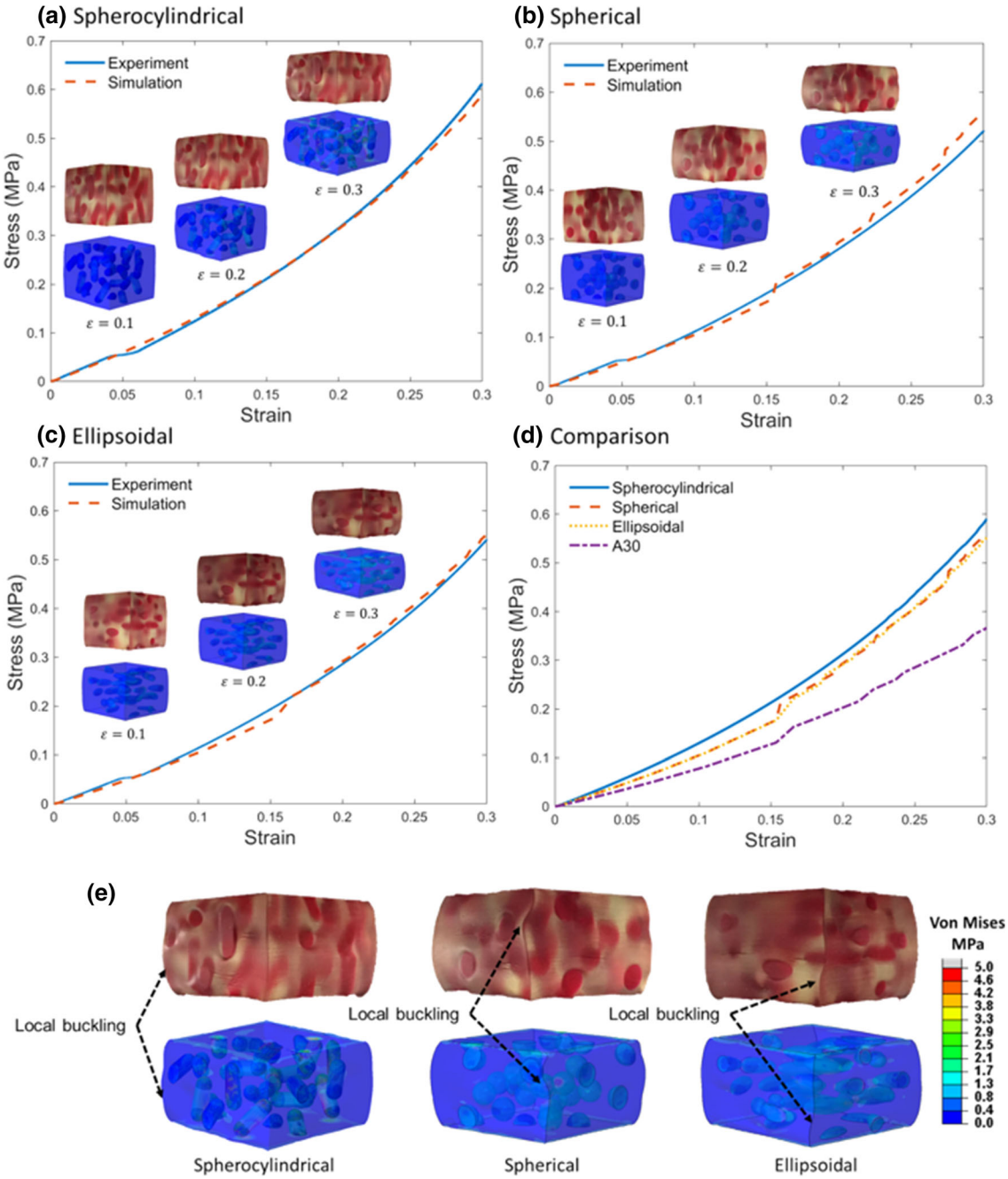

Fig. 12. Comparison of numerical simulation with experimental results for A30 cubic with (a) spherocylindrical, (b) spherical and (c) ellipsoidal reinforcements. (d) Comparison of pure A30 cubic with composite cubic. (e) Comparison of experiments and numerical simulations at strain $\varepsilon = 0.3$.

the A30 matrix are well captured in the numerical simulation. For engineering strain > 0.25, the engineering stress predicted by simulation are slightly higher than the observed values from experiments for spherical and ellipsoidal reinforcements. This could be attributed to the slight damage that occurred during the experiment, which was not considered in the numerical model. As shown in Fig. 12d, the stress developed on the VMV particles is noticeably higher than on the A30 matrix, which indicates that the introduction of VMV particles helps to reinforce the A30 matrix in the composite. Figure 12c presents the comparison of pure A30 cubic and A30 with different reinforcement particles under compression. It is clear that the reinforced A30 cubic is much stiffer than pure A30 samples. Among the different reinforcements investigated, the spherocylindrical

particle-reinforced composite shows the best performance in terms of mechanical strength, while the spherical and ellipsoidal ones give similar results. It should be noted that the three cases have the same volume fraction of particles. Overall, the results suggest that the introduction of VMV particles in the A30 matrix can lead to enhancement of mechanical properties.

CONCLUSION

In this work, we explored the potential of the Stratasys J750 to produce bi-material 3D additively manufactured or 3D-printed parts.

(a) From the macroscopic point of view, both parallel and transverse printing directions had a limited effect on the strength of the homogeneous (single material) samples.
(b) Heterogeneous (bi-material) tensile samples failed at the gauge section, and no delamination was observed. However, there were distinct localised fracture areas in the tensile samples originating from the matte surfaces facing the print platform and progress toward the upper glossy surfaces. This failure pattern indicated the sample properties may not be uniform across the thickness and further investigation is required to determine the level of variation. The curvature of the matte surface was also observed and could be attributed to the residual stress built up across the thickness; however, this further study needs to be done to determine the origin and influences of residual stress on mechanical properties.
(c) The introduction of VeroMagentaV particles in the Agilus30 matrix had a noticeable strengthening effect on the composite compression samples.
(d) On a microstructural level, our results proved that bi-material printing via material jetting does not necessary fail at the interface. However, visual inspections on the fracture surfaces show that the matte surface created as a by-product of the AM process induced crack initiation leading to the final failure. Print orientation needs to be carefully considered to avoid the effects of the matte surface on the samples.
(e) The numerical simulation presented here captured the deformation of the composite samples very well. With the similar volume fraction of reinforcements, the spherocylindrical particles gave the highest strengthening effect, while spherical and ellipsoidal particles gave similar responses. The appearance of these particles clearly affected the local deformation of the Agilus30 cube, and the buckling modes were captured very well.

ACKNOWLEDGEMENTS

The authors acknowledge the facilities and the scientific and technical assistance of the Advanced Manufacturing Precinct. This work is supported by Vingroup Innovation Foundation (VINIF) in project code VINIF.2019.DA04. Authors also acknowledge the Australian Microscopy & Microanalysis Research Facility and the Rheology and Materials Characterisation Laboratory at RMIT University.

REFERENCES

1. K.C. Nguyen, P. Tran, and H.X. Nguyen, *Autom. Constr.* 99, 79 (2019).
2. P. Tran, T.D. Ngo, A. Ghazlan, and D. Hui, *Compos. Part B* 108, 210 (2017).
3. A. Bandyopadhyay and B. Heer, *Mater. Sci. Eng. R* 129, 1 (2018).
4. H. Yang, J.C. Lim, Y. Liu, X. Qi, Y.L. Yap, V. Dikshit, W.Y. Yeong, and J. Wei, *Virtual Phys. Prototyp.* 12, 95 (2017).
5. Stratasys, SUP706/SUP706B Support Material. http://www.stratasys.com (2019).
6. J. Mueller, S. E. Kim, K. Shea and C. Daraio, in *Proceedings of the ASME 2015 International Design Engineering Technical Conferences and Computers and Information in Engineering Conference*, V01AT02A040-V001AT002A040 (2015).
7. J. Mueller, D. Courty, M. Spielhofer, R. Spolenak, and K. Shea, *3D Print Addit. Manuf.* 4, 193 (2017).
8. A. Cazon, P. Morer, and L. Matey, *Proc. Inst. Mech. Eng. Part B* 228, 1664 (2014).
9. J.W. Stansbury and M.J. Idacavage, *Dent. Mater.* 32, 54 (2016).
10. M. Sugavaneswaran and G. Arumaikkannu, *Mater. Des.* 54, 779 (2014).
11. L. Bass, N.A. Meisel, and C.B. Williams, *Rapid Prototyp. J.* 22, 826 (2016).
12. G. Loh and E. Pei, *Proceedings of the 15th Rapid Design, Prototyping and Manufacturing Conference*, Northumbria University, (2017).
13. G.H. Loh, E. Pei, D. Harrison, and M.D. Monzon, *Addit. Manuf.* 23, 34 (2018).
14. J.P. Moore and C.B. Williams, *Rapid Prototyp. J.* 21, 675 (2015).
15. T.S. Lumpe, J. Mueller, and K. Shea, *Mater. Des.* 162, 1 (2019).
16. Z. Quan, A. Wu, M. Keefe, X. Qin, J. Yu, J. Suhr, J.-H. Byun, B.-S. Kim, and T.-W. Chou, *Mater. Today* 18, 503 (2015).
17. J.-Y. Lee, J. An, and C.K. Chua, *Appl. Mater. Today* 7, 120 (2017).
18. L.S. Dimas, G.H. Bratzel, I. Eylon, and M.J. Buehler, *Adv. Funct. Mater.* 23, 4629 (2013).
19. A.S. Dalaq, D.W. Abueidda, and R.K.A. Al-Rub, *Compos. A* 84, 266 (2016).
20. X. Chen, I. Ashcroft, C. Tuck, Y. He, R.J. Hague, and R.D. Wildman, *J. Mater. Res.* 32, 1407 (2017).
21. S.Y. Hong, Y.C. Kim, M. Wang, H.-I. Kim, D.-Y. Byun, J.-D. Nam, T.-W. Chou, P.M. Ajayan, L. Ci, and J. Suhr, *Polymer* 145, 88 (2018).
22. F. Libonati, G.X. Gu, Z. Qin, L. Vergani, and M.J. Buehler, *Adv. Eng. Mater.* 18, 1354 (2016).
23. I. Vu, L. Bass, N. Meisel, B. Orler, C.B. Williams and D.A. Dillard, *Proceedings of the Solid Freeform Fabrication Symposium Proceedings*, pp. 959–982 (2014).
24. K. Wang, C. Wu, Z. Qian, C. Zhang, B. Wang, and M.A. Vannan, *Addit. Manuf.* 12, 31 (2016).
25. T. Li, Y. Chen, X. Hu, Y. Li, and L. Wang, *Mater. Des.* 142, 247 (2018).
26. J. Bennett, *Addit. Manuf.* 18, 203 (2017).
27. J. Mueller, K. Shea, and C. Daraio, *Mater. Des.* 86, 902 (2015).

28. Stratasys, PolyJet Materials Data Sheet. http://www.stratasys.com (2014).
29. M.C. Boyce and E.M. Arruda, *Rubber Chem. Technol.* 73, 504 (2000).
30. G. Marckmann and E. Verron, *Rubber Chem. Technol.* 79, 835 (2006).
31. F. Fischer, *POP Plast. Packag.* 60, 2050 (2015).
32. A.T. Gaynor, N.A. Meisel, C.B. Williams, and J.K. Guest, *J. Manuf. Sci. Eng.* 136, 061015-1 (2014).
33. A. Standard, *Annu. Book ASTM Stand.* 8, 1 (2009).
34. W. Wang and K. Lu, *J. Mater. Res.* 17, 2314 (2002).
35. M. R. VanLandingham, J. S. Villarrubia, W. F. Guthrie and G. F. Meyers, *Proceedings of the Macromolecular Symposia*, pp. 15–44 (2001).
36. F. Wang, L. Wang, Q. Yang, and J. Li, US Patent No. US20180312707A1 (2018).
37. E.M. Arruda and M.C. Boyce, *J. Mech. Phys. Solids* 41, 389 (1993).